Draft version June 24, 2022
Typeset using LaTeX **twocolumn** style in AASTeX631

SN 2020jgb

Authors[1]

[1] *Center for Interdisciplinary Exploration and Research in Astrophysics (CIERA), Department of Physics and Astronomy, Northwestern University, 1800 Sherman Road, Evanston, IL 60201, USA*

ABSTRACT

Keywords: keywords

1. INTRODUCTION

It has been clear for decades that Type Ia Supernovae (SNe Ia) are caused by the thermonuclear explosions in carbon-oxygen (C/O) white dwarfs (WDs) in binary systems (see Maoz et al. 2014, for a review). Nevertheless, the nature of the binary companion, as well as how it ignites the WD, remains highly uncertain.

The helium-shell (He-shell) double detonation (DDet) scenario is one of the most promising channels to produce SNe Ia. In this scenario, the WD accretes from a companion to develop a helium-rich shell, which, once becomes massive enough, could detonate. Such a detonation sends a shock wave into the C/O core to trigger a runaway thermonuclear explosion and inevitably destroy the whole WD (Nomoto 1982a,b; Woosley et al. 1986; Livne 1990; Woosley & Weaver 1994; Livne & Arnett 1995), even when the WD is below the Chandrasekhar mass ($M_{\rm Ch}$).

There are several observational benchmarks for He-shell DDet triggered SNe. Shortly after the ignition of the shell, the decay of radioactive material in the helium ashes may power a detectable flash (Bildsten et al. 2007; Fink et al. 2010; Kromer et al. 2010). The Fe-group elements in the ashes will blanket blue photons with wavelengths $\lesssim$5000 Å (Kromer et al. 2010), the duration of which depends on the mass of the He-shell. For thick enough shells, Boyle et al. (2017) suggest that the unburnt helium could provide observational signal in near infrared (NIR) spectra, and Polin et al. (2021) predict significant [Ca II] emission in the nebular phase of the SNe.

Using different combos of He-shell mass and C/O core mass, one can reproduce a variety of observables in 'normal' SNe Ia with typical luminosities and spectral features near peak light, or peculiar sub-luminous ones (Polin et al. 2019).

For the DDet SNe that show 'normal' characteristics near their peaks, the mass of the He-shell is expected to be low ($\lesssim$0.03 $\mathrm{M}_\odot$; Kromer et al. 2010; Sim et al. 2010; Shen et al. 2018; Polin et al. 2019). The first DDet candidate with a thin He-shell is SN 2016jhr (Jiang et al. 2017), which exhibits an early red flash and keeps a red $g-r$ color throughout its evolution, though it show a typical absolute magnitude at peak ($M_g \approx -19$) for normal SNe Ia. The multi-band light curves involving the early flash and the major peak, as well as the optical spectrum close to the peak light, could be simultaneously fit by a near-$M_{\rm Ch}$ DDet model (a 1.38 $\mathrm{M}_\odot$ C/O core and a 0.03 $\mathrm{M}_\odot$ He-shell). Recently, a thinner He-shell is discovered in SN 2018aoz (Ni et al. 2022), a SN Ia showing a rapid redward color evolution within $\approx$12 hr after the first light, which could be explained by a sub-$M_{\rm Ch}$ DDet model (a 1.05 $\mathrm{M}_\odot$ C/O core and a 0.03 $\mathrm{M}_\odot$ He-shell). After this red excess the photometry evolution is consistent with normal SNe Ia, when the ashes of the thin He-shell becomes optically thin. To date, only a small fraction of SNe Ia have been discovered early enough for possible detection of early flashes (e.g., Deckers et al. 2022). While there could be a large underlying population of normal SNe Ia triggered by He-shell DDet, it is hard to prove so.

In contrast, if the He-shell mass is much greater than 0.03 $\mathrm{M}_\odot$, the ashes of the He-shell detonation could remain optically thick in a much more extended phase, resulting in the red color and low luminosity near peak light. SN 2018byg (De et al. 2019) is a prototype of thick He-shell DDet SNe. During the late stages of preparing for this paper, Dong et al. (2022) presented another thick shell He-shell DDet candidates, SN 2016dsg, accompanied with an archival transient OGLE-2013-SN-079 (Inserra et al. 2015). All three candidates are faint, red, and show strong line-blanketing near peak lights. Dong et al. (2022) also report tentative detection of unburnt helium in SN 2016dsg. The small sample size to date suggests thick shell events might be intrinsically rare.

It has been suggested that some, if not all, of the calcium-rich (Ca-rich) gap transients, a population of faint SNe with conspicuous [Ca II] emission in the nebular phase, also arise from He DDet (Dessart & Hillier 2015; De et al. 2020; Polin et al. 2021). A subclass of Ca-rich transients resemble SNe Ia near peak lights (termed Ca-Ia objects), marked by the strong Si II absorption and the absence of optical He I lines. There are only two Ca-Ia objects (SN 2016hnk and SN 2019ofm; De et al. 2020), both showing significant line-blanketing in spectra, and hence could be He-shell DDet objects. Nonetheless, they also exhibit properties of other types of sub-luminous SNe Ia, such as the strong O I absorption widely seen in 91bg-like objects (Filippenko et al. 1992) but not in other He-shell DDet candidates. Galbany et al. (2019) argue that SN 2016hnk is also consistent with a 91bg-like object arising from the deflagration of a near-$M_{\rm Ch}$ WD. In a word, the nature of Ca-Ia objects remain ambiguous. **Mention red Ca-Ib/c?**

In this paper, we present the observations of another promising candidate of a thick He-shell DDet SN, SN 2020jgb. This peculiar SN Ia highly resembles SN 2018byg in photometric and spectroscopic properties, and exhibits a remarkable feature in the NIR spectrum that could be attributed to the unburnt helium. In Section 2 we report the observations of SN 2020jgb, which are analyzed in Section 3, where we show its similarities with other He-shell DDet SNe and discuss the tentative He I absorption features. We use a grid of DDet models to fit the data of SN 2020jgb, and present the results in Section 5. In Section 4 we discuss the diversity in the host environments of DDet events. We draw our conclusions in Section 6.

2. OBSERVATIONS

2.1. *Discovery*

SN 2020jgb was first discovered by the Zwicky Transient Facility (ZTF; Bellm et al. 2019; Graham et al. 2019) on 2020 May 03.463 UT (MJD 58972.463) with the 48-inch Samuel Oschin Telescope (P48) at Palomar Observatory. The automated ZTF discovery pipeline (Masci et al. 2019) detected SN 2020jgb using the image-differencing technique of Zackay et al. (2016). The candidate passed internal thresholds (e.g., Mahabal et al. 2019; Duev et al. 2019), leading to the production and dissemination of a real-time alert (Patterson et al. 2019) and the internal designation ZTF20aayhacx. It was detected at a magnitude of 19.86 in the $g_{\rm ZTF}$-band, and J2000 coordinates $\alpha = 17^{\rm h}53^{\rm m}12^{\rm s}.651$, $\delta = -00^\circ51'21''.81$ and announced to the public in Fremling (2020). The host galaxy, PSO J175312.663+005122.078, is a dwarf galaxy, to which SN 2020jgb has a projected offset of only $0.3''$. The last non-detection was on 2020 April 27.477 (MJD 58966.477; 5.99 days before the first detection) up to a limiting magnitude of 20.7 in the $r_{\rm ZTF}$-band. This transient was identified as a SN Ia by Dahiwale & Fremling (2020) due to the prominent Si II absorption features and a lack of any H features in the spectrum obtained on 2020 May 28.468.

2.2. *Optical Photometry*

SN 2020jgb was monitored in the $g_{\rm ZTF}$ and $r_{\rm ZTF}$-bands by ZTF as part of its ongoing Northern Sky Survey (Bellm et al. 2019). We adopt a Galactic extinction of $E(B-V) = 0.404$ mag (Schlafly & Finkbeiner 2011), and correct all photometry using the Fitzpatrick (1999) extinction model. We assume there is no additional extinction in the host galaxy. This assumption is supported by the lack of Na I D absorption at the redshift of the host galaxy, though see Poznanski et al. (2011) for caveats on the use of Na I D absorption as a proxy for extinction.

To get the distance modulus to SN 2020jgb, we use the 2M++ model (Carrick et al. 2015) to obtain a peculiar velocity towards its host galaxy, PSO J175312.663+005122.078, to be $179\,{\rm km\,s^{-1}}$. This, combined with the recession velocity in the frame of the cosmic microwave background[1] (CMB) $v_{\rm CMB} = 9136\,{\rm km\,s^{-1}}$, give a net Hubble recession velocity is $9307\,{\rm km\,s^{-1}}$ [AAM: uncertainty?]. Adopting $H_0 = 70\,{\rm km\,s^{-1}\,Mpc^{-1}}$, $\Omega_M = 0.3$, and $\Omega_\Lambda = 0.7$, we estimate the luminosity distance to SN 2020jgb to be 136.1 Mpc, which yields a distance modulus of $\mu = 35.66$.

The forced photometry light curves (absolute magnitudes) in $g_{\rm ZTF}$- and $r_{\rm ZTF}$-bands are shown in Figure 1, in which we show all the measurements with SNR > 2.

2.3. *Optical Spectroscopy*

We obtained optical spectroscopic follow-up of the object from ~-10 days to $\sim+150$ days relative to the $r_{\rm ZTF}$-band peak, using the Spectral Energy Distribution Machine (SEDM; Blagorodnova et al. 2018) on the automated 60 inch telescope (P60; Cenko et al. 2006) at Palomar Observatory, the Kast Double Spectrograph (Miller & Stone 1994) at the Shane 3 m Telescope, the Andalucia Faint Object Spectrograph and Camera (ALFOSC)[2] installed at the Nordic Optical Telescope (NOT), the Double Beam Spectrograph (DBSP) on the 200 inch Hale telescope (P200; Oke & Gunn 1982), the Low Resolution Imaging Spectrograph (LRIS) on the Keck I telescope (Oke et al. 1995). Spectra were reduced using

[1] See https://ned.ipac.caltech.edu/velocity_calculator.

[2] https://www.not.iac.es/instruments/alfosc/

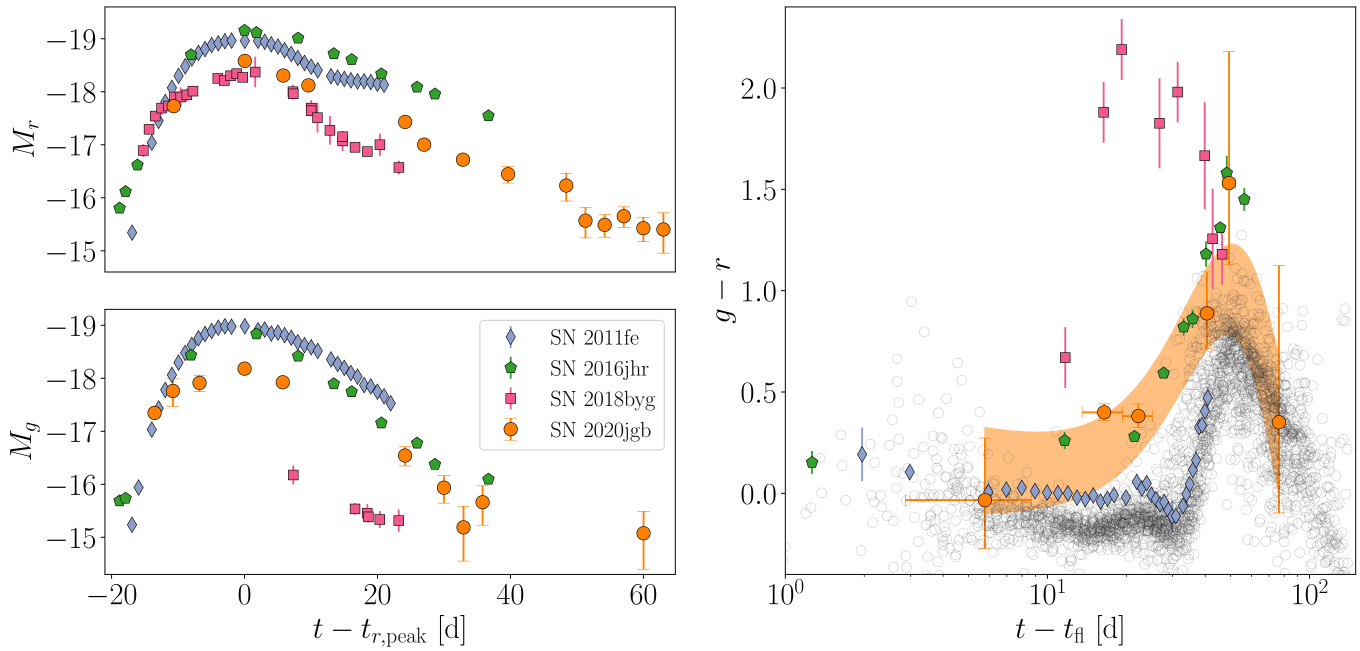

Figure 1. *Left*: Comparison of the multi-color light curves of SN 2020jgb with the normal SN Ia SN 2011fe, the thin shell DDet candidate SN 2016jhr, and the thick shell DDet candidate SN 2018byg. The upper (lower) panel shows the evolution in g-band (r-band) absolute magnitudes. *Right*: comparison of $g-r$ color evolution to SN 2011fe and SN 2018byg, as well as 62 normal SNe Ia (open circles) with prompt observations within 5 days of first light by ZTF (Bulla et al. 2020). The shaded region denotes the 1-σ credible interval of the color of SN 2020jgb until ∼60 days after the peak, estimated using Gaussian process.

standard procedures (e.g., Matheson et al. 2000). Details of the spectroscopic observations are listed in Table 1, and the spectral sequence is shown in Figure 2.

On 2022 March 31, two years after the transient faded, we also took a spectrum for its host galaxy using the DEep Imaging Multi-Object Spectrograph (DEIMOS) on the Keck II telescope (Faber et al. 2003), for a total integration time of 3200 s. The spectra were reduced with the `PypeIt` Python package (Prochaska et al. 2020).

2.4. *Near-infrared (NIR) Spectroscopy*

We obtained one NIR (0.8-2.5 μm) spectrum of SN 2020jgb using the Gemini near-infrared spectrometer (GNIRS; Elias et al. 1998) on the Gemini North telescope on 2020 June 9 (∼22 days after r_{ZTF}-band peak), for an integration time of 2400 s. The GNIRS spectrum was reduced with the `PypeIt` package.

Table 1. Spectroscopic Observations of SN 2020jgb and the host galaxy.

t_{obs} (MJD)	Phase (d)	Telescope/ Instrument	R ($\lambda/\Delta\lambda$)	Range (Å)	Air Mass
58,976.42	−9.7	P60/SEDM	100	3770–9220	1.23
58,982.12	−4.2	NOT/ALFOSC	360	4000–9620	1.17
58,990.43	+3.9	P60/SEDM	100	3770–9220	1.23
58,997.44	+10.7	P60/SEDM	100	3770–9220	1.29
58,998.41	+11.6	Shane/Kast	750	3620–10720	1.28
59,008.41	+21.3	P60/SEDM	100	3770–9220	1.28
59,009.45	+22.4	Gemini-N/GNIRS	1800	8230–25150	1.07
59,010.40	+23.3	P200/DBSP	700	3200–9500	1.27
59,023.58	+36.1	Keck I/LRIS	1100	3200–10250	2.04
59,107.29	+117.3	Keck I/LRIS	1100	3200–10250	1.31
59,143.26	+152.2	Keck I/LRIS	1100	3200–10250	2.16
59,669.60	host	Keck II/DEIMOS	2100	4500–8700	1.14

Note—Phase is measured relative to the r_{ZTF}-band peak in the host galaxy rest frame. The resolution R is reported for the central region of the spectrum.

3. ANALYSIS

3.1. *Photometric Properties*

SN 2020jgb exhibited a fainter light curve than normal SNe Ia. In Figure 1, we compare the photometric properties of SN 2020jgb with the nearby, well-observed SN 2011fe (Nugent et al. 2011) and two He-shell DDet candidates, including the normal-luminosity thin shell candidate SN 2016jhr (Jiang et al. 2017) and the sub-luminous thick shell candidate SN 2018byg (De et al.

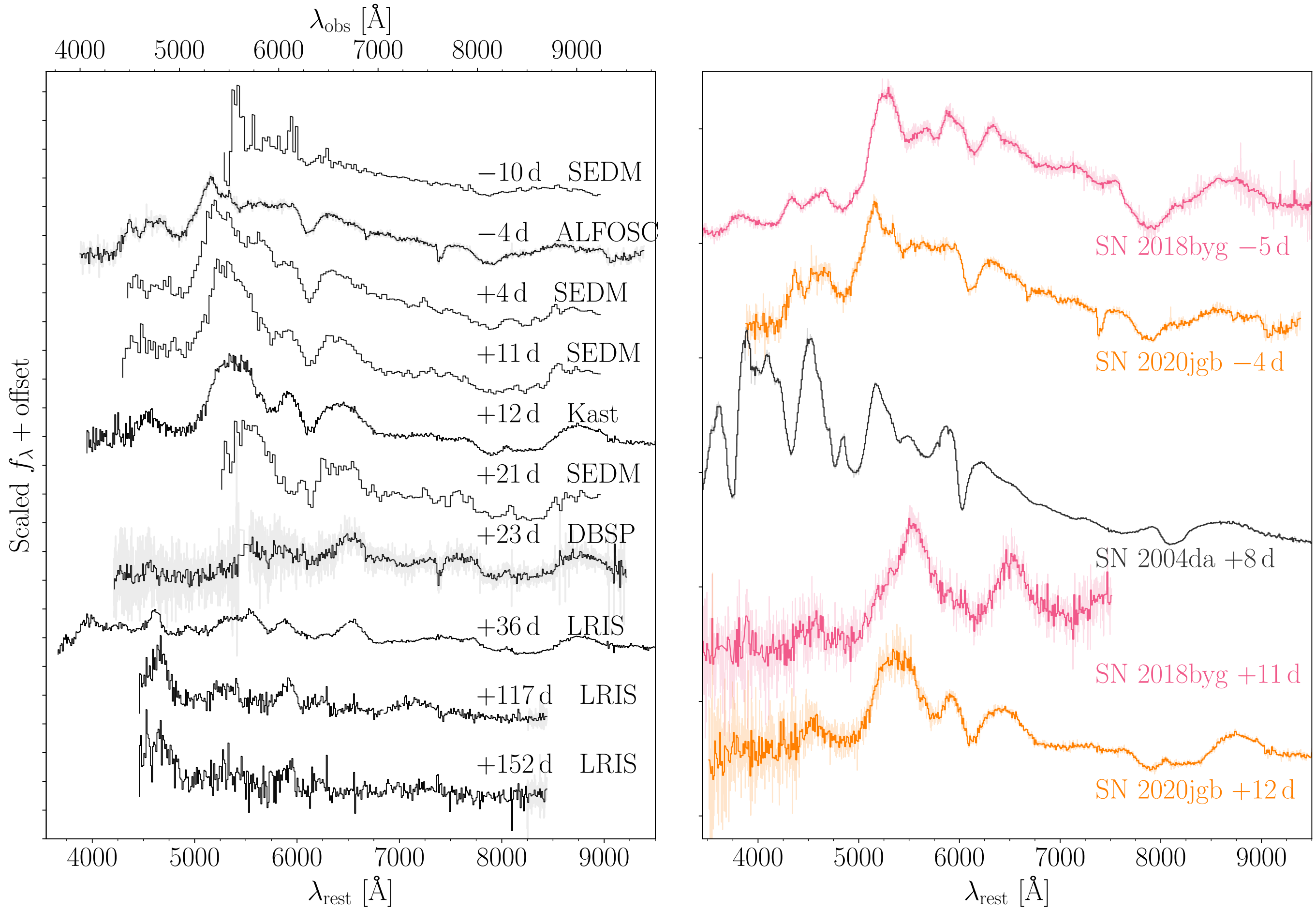

Figure 2. *Left*: optical spectral sequence of SN 2020jgb. Rest frame phases (days) relative to the $r_{\rm ZTF}$-band peak and instruments used are posted next to each spectrum. The spectra are after Galactic extinction correction are shown in grey. The black lines are binned spectra with a bin size of 10 Å, except for the SEDM spectra, whose resolution is lower than the bin size. In the last two spectra, we have subtracted the light from the host galaxy. Only regions with SNR $>$ 2.5 after binning are plotted. *Right*: spectral comparison with SN 2018byg (sub-luminous He-shell DDet) and SN 2004da (normal luminosity). Spectra for SN 2004da and SN 2018byg are obtained from the WISEReP repository (Yaron & Gal-Yam 2012).

2019), with available photometric data on the Open Supernova Catalog[3] (Guillochon et al. 2017).

The first detection was made on MJD=58972.46 in the $g_{\rm ZTF}$-band. Before $\sim$−15 days relative to the peak light, the luminosity of SN 2020jgb is similar to the canonical object SN 2011fe and also the two DDet candidates. But within the two weeks before the peak, SN 2020jgb brightens by only $\approx$0.6 mag in the $g_{\rm ZTF}$-band, while SN 2011fe brightens by $\approx$2.0 mag in the g-band. Near the peak, the DDet sample is heterogeneous in luminosity. The decline rates also show diversity in both bands.

In the right panel of Figure 1, we also compare the color evolution ($g-r$) of these objects as measured from their first light $t_{\rm fl}$, accompanied by 62 normal SNe Ia (open circles) observed within 5 days of $t_{\rm fl}$ by ZTF (from Bulla et al. 2020). For SN 2020jgb the early rise of the light curve was not well sampled, so we take the midpoint of the first detection and the last non-detection as an approximation of the first light time $t_{\rm fl}$, with the uncertainty ($\approx$3 days) being half of the offset between these two epochs. We also estimate the 1-σ uncertainty of the $g_{\rm ZTF} - r_{\rm ZTF}$ color (the shaded region) in SN 2020jgb by fitting the forced photometry light curves in individual bands with Gaussian process (GP). The GP regression is conducted with the `gaussian_process` module in the `scikit-learn` package (Pedregosa et al. 2011), in which a combination of the radial-basis function (RBF) kernel and the white kernel is adopted. Measurements with lower SNR ($1 <$ SNR < 2) are also included in the fit to better model the decline in both bands $\gtrsim$30 days after the peak. All three DDet candi-

[3] See https://github.com/astrocatalogs/supernovae.

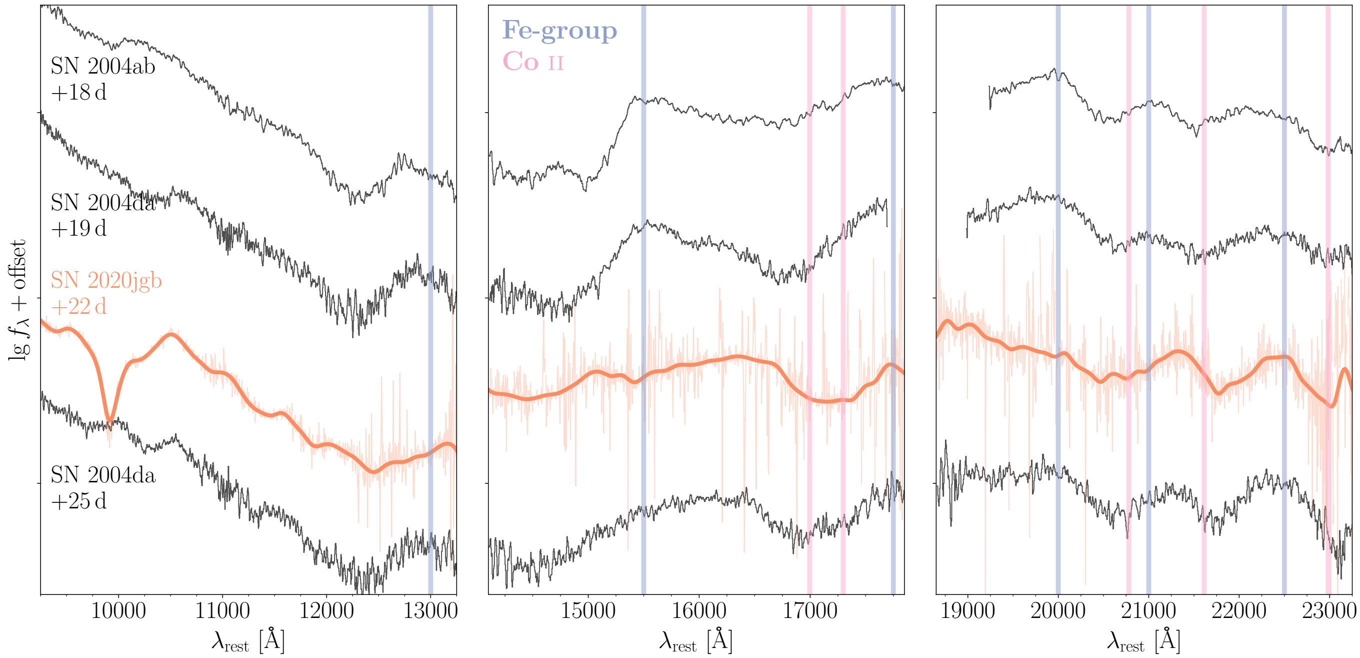

Figure 3. The NIR spectra of SN 2020jgb and two SNe Ia with normal maximum luminosity (SN 2004ab and SN 2004da, Marion et al. 2009), taken about three weeks after the peak. For each spectrum, the continuum at $\gtrsim 1.2\,\mu$m is significantly reshaped by the Fe-group blanketing (emission features, blue vertical lines) and Co II absorption (pink vertical lines). Spectra for SN 2004ab and SN 2004da are obtained from Marion et al. (2009).

dates are undoubtedly redder than normal SNe Ia. At peak light, SN 2020jgb was not as red as the extreme case, SN 2018byg ($g_{\rm ZTF} - r_{\rm ZTF} \approx 2.2$), but exhibited a similar color as SN 2016jhr ($g - r \approx 0.5$).

3.2. *Optical Spectral properties*

In Figure 2, we show the optical spectral sequence of SN 2020jgb, and compare its spectra with some other SNe Ia near peak luminosity. For the spectra obtained after +100 d there is clear contamination from the host-galaxy, including the presence of narrow emission lines. For these spectra we have subtract the galaxy light as measured in the DEIMOS spectrum from 2022 (see Section 2.3). The earliest spectrum was obtained by SEDM ≈10 days before the $r_{\rm ZTF}$-band peak. We only show portions of the spectrum where the SNR > 2.5, where the continuum is almost featureless with some marginal detection of the Si II λ6355 at ≈6100 Å, the trademark of SNe Ia. In subsequent spectra the Si II features become more prominent and are clearly detected through +12 d. To get the expansion velocity, following Maguire et al. (2014), we fit the Si II feature with a Gaussian profile. We first select the absorption region by visual inspection. The continuum is assumed to be linear. The continuum flux density at blue and red edges are also set to be free parameters, whose priors are Gaussian distributions, where the means are the flux density measured at each edge and the standard deviations are the corresponding flux uncertainties. The absorption feature is then normalized by the continuum and fit to a single Gaussian profile with three parameters (amplitude, mean velocity, velocity dispersion). Posteriors of these five parameters are sampled with `emcee` (Foreman-Mackey et al. 2013) using the Markov chain Monte Carlo (MCMC) method. We estimated the mean expansion velocity to be ≈11,500 km s^{-1} near peak light.

In many SNe Ia, the spectral absorption features by Ca II infrared triplet (IRT) have two distinct components, namely the photospheric-velocity features (PVFs) and high-velocity features (HVFs). The PVFs originate from the main line-forming region with typical photospheric (i.e., bulk ejecta) velocities, while the HVFs are blueshifted to much shorter wavelengths, indicating significantly higher (by greater than ∼6000 km s^{-1}) velocities than typical PVFs (Silverman et al. 2015). SN 2020jgb has prominent HVFs of Ca II IRT. In the earliest spectrum, the wide HVFs at about 7800-8200 Å already become visible. Using the similar technique in modeling the Si II features, we fit the HVFs with multiple Gaussian profiles assuming each line in the triplet can be approximated by the same profile (i.e., same amplitude and velocity dispersion), and obtained a best-fit expansion velocity $\gtrsim$26,000 km s^{-1}. Such HVFs remain visible for over 40 days. The PVFs for Ca II IRT at about 8200-8600 Å is not visible until in our second spectrum ≈4 days before peak light. Since then we fit the broad absorption features with two different velocity components simultaneously. The velocity of HVFs slightly declines but stays above $\approx$24,000 km s^{-1}, and the velocity of PVFs declines from $\approx$11,000 km s^{-1} to $\approx$9,000 km s^{-1}. As in normal SNe Ia, the relative strength between HVFs and PVFs decreases with time.

The nebular phase spectra of SN 2020jgb are dominated by the Fe-group elements, showing some enhancement in flux between $\approx$4500 and $\approx$6000 Å. We did not detect any emission feature related to [Ca II] $\lambda\lambda$7291, 7324, which is a hallmark for Calcium-rich gap transients and is also prominent in a few DDet candidates (e.g., SN 2016hnk and SN 2019ofm; De et al. 2020).

The spectral evolution of SN 2020jgb in the optical strongly resembles SN 2018byg, a sub-luminous DDet candidate with a potentially thick helium shell. At early times, both SNe were relatively blue and featureless with broad and shallow Ca II IRT absorption. As they evolved closer to maximum light, they developed strong continuous absorption bluewards of $\approx$5000 Å, while the Si II λ6355 and the Ca II IRT became more prominent. S II was not detected in either object. In the DDet scenario, a large amount of Fe-group elements will be synthesized in the outer regions of the ejecta, which will cause significant line-blanketing near peak light (Kromer et al. 2010; Polin et al. 2019), and also high velocity intermediate-mass elements like Ca II (Fink et al. 2010; Kromer et al. 2010). This makes SN 2020jgb another promising candidate for DDet SN with a thick helium shell.

SN 2004da is a normal SN Ia that shows similarities to SN 2020jgb in the NIR (Section 3.3), however, the two SNe are extremely different in the optical approximately 10 d after maximum light (Figure 2). From this comparison it is clear that SN 2020jgb is not a normal SN Ia.

3.3. *NIR Spectral properties*

The NIR spectrum of SN 2020jgb is compared with two normal SNe Ia at a similar phase in Figure 3 (data for SNe 2004ab and 2004da from Marion et al. 2009). SN 2020jgb shows a strong absorption feature at $\sim$0.99 μm, which is not seen in normal SNe Ia. This feature was still significant two weeks later, as detected by LRIS on Keck (see Figure 4), though it was only partially covered. In general, SN 2020jgb highly resembles normal SNe Ia in NIR band. The shape of the continuum redwards to $\approx$1.2 μm is significantly altered by line-blanketing of Fe-group elements synthesized in the SN interior, as opposed to the Fe-group elements in the outermost region as ashes of shell helium burning. Just like normal SNe Ia, SN 2020jgb shows an enhancement of flux at about 1.3, 1.55, 2.0, 2.1, and 2.25 μm, accompanied by several Co II absorption lines. It is especially similar to SN 2004da at +25 days after maximum as the steep increase in flux at $\approx$1.55 μm, known as the *H*-band break (Hsiao et al. 2019), has become less prominent.

What is not seen in usual SNe Ia is the wide, deep absorption at $\sim$0.99 μm (hereafter the 1 μm feature), indicating its peculiarity. According to Marion et al. (2009), normal SNe Ia are nearly featureless in spectra around 1 μm a few weeks after maximum light. There are several elements that may be associated with this feature, however, none of them provide a fully satisfying explanation. Below, we discuss the origin of the peculiar 1 μm feature.

The most tantalizing possibility is that the absorption is due to He I λ1.0830 μm. If SN 2020jgb is a DDet SN, then unburned He could lead to observed absorption in the spectrum, as shown in the sub-Chandrasekhar-mass He-shell DDet models of (Boyle et al. 2017). Figure 4 shows that the 1 μm feature, if associated with He I λ1.0830 μm, has a high velocity ($\sim$26,000 km s^{-1}), especially considering the phase of the SN. The Ca II IRT also exhibits similarly high velocities at the same phase ($\sim$24,000 km s^{-1}), meaning it is possible to see absorption at such velocities well after maximum light. The expansion velocity in the ejecta is roughly linearly proportional to the radius, so such a high velocity indicates that both the Ca II IRT and the tentative He I absorption line form far outside the normal photosphere, which has a velocity of only $\approx$10,000 km s^{-1}. In the sense, the He-shell DDet scenario, in which the unburnt helium locates at the outermost ejecta, is indeed supported.

Still, this helium detection remains skeptical, since other He I are not unambiguously detected, such as the He I λ2.0581 μm. Considering a line velocity of $\approx$26,000 km s^{-1} and a host galaxy redshift of 0.0309, this line will be blueshifted to $\approx$1.95 μm in the observer frame, so will be strongly blended by the strong telluric lines within 1.8-2.0 μm. After telluric correction, the signal to noise ratio reaches $\sim$5, with which we still cannot see any significant absorption feature. An upper limit of the equivalent width is determined to be $<$2% of the 1.0830 μm line, while theoretically, the 2.0581 μm line is supposed to be only a factor of 6-12 weaker, depending on temperature (Marion et al. 2009). Another fact is that the 1 μm feature is as strong as the He I λ1.0830 μm in many helium-rich core-collapse supernovae, say, Type Ib supernovae, in which the He I λ2.0581 μm is weaker than the 1.0830 μm line yet still prominent (Shahbandeh et al. 2022). If the 1 μm feature is associated with He I, it would be very unusual if the 2 μm feature is not seen at all, even if somehow blended by the telluric lines.

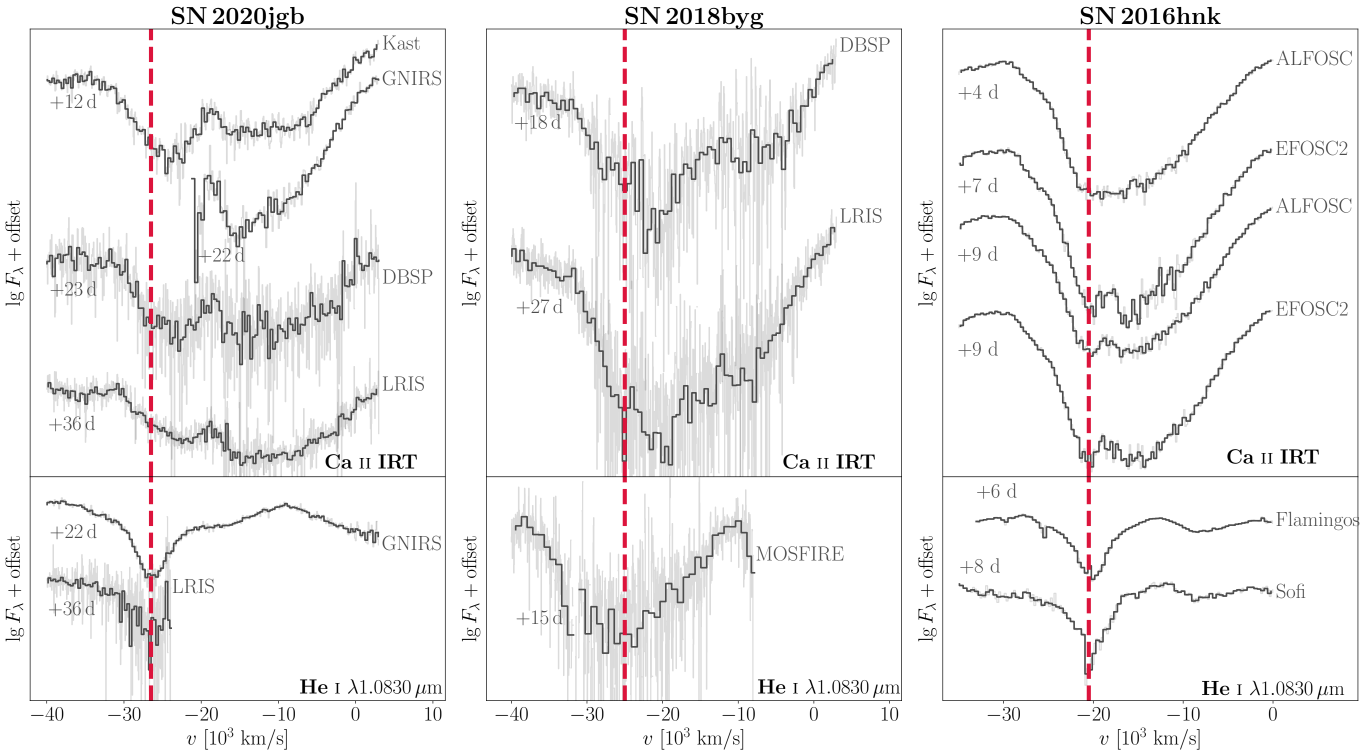

Figure 4. Spectra of SN 2020jgb, SN 2018byg, and SN 2016hnk in the velocity space, comparing the Ca II IRT absorption features (upper panels) and the $1\,\mu$m features assuming they are associated with He I $\lambda 1.0830\,\mu$m (lower panels). The red dashed lines mark the minimum of each $1\,\mu$m feature. Data for SN 2018byg and SN 2016hnk are obtained from the WISEReP repository (Yaron & Gal-Yam 2012).

[Chang: There should be a note here about the strength of the lines in the Boyle paper... for one of their models there is no obvious 2 micron absorption] [AAM: that model is for 'normal' SNe Ia]

Other possibilities include the Mg II $\lambda 1.0927\,\mu$m, the C I $\lambda 1.0693\,\mu$m, and the Fe II $\lambda 1.0500\,\mu$m & $\lambda 1.0863\,\mu$m. The Mg II $\lambda 1.0927\,\mu$m line is prevalent in the NIR spectra of SNe Ia, but usually disappears within a week after the peak luminosity (Marion et al. 2009), while the $1\,\mu$m feature was still visible over a month after the peak in the Keck LRIS spectrum. The required radial velocity is $\approx$30,000 km s^{-1}, $\approx$20% faster than the HVFs of Ca II IRT at the same phase. While such a high velocity for Mg II has never been seen in other SNe Ia, since high-velocity intermediate-mass elements like magnesium and calcium can be synthesized by the detonation of helium shell (Shen & Moore 2014), the Mg II origin of the $1\,\mu$m feature cannot be strictly ruled out. But if we attribute this $1\,\mu$m feature to high-velocity Mg II, we would expect an even stronger $\lambda 0.9227\,\mu$m line to be blueshifted to the red edge of the Ca II IRT, which is not detected. Given the strength of the $1\,\mu$m feature, the $0.9227\,\mu$m line should not be completely obscured by the Ca II IRT features.

The C I $\lambda 1.0693\,\mu$m line from the unburnt carbon is much less frequently seen than the Mg II $\lambda 1.0927\,\mu$m. Hsiao et al. (2019) presented a sample of five SNe Ia with C I detections, showing the C I feature is strongest for those fainter, fast-declining objects. However, in their sample, the C I feature is a pre-maximum feature which fades away as the luminosity peaks, so the discrepancy in phase is large. The required expansion velocity $\approx$22,000 km s^{-1}, which is overwhelmingly faster than the estimated carbon velocity for the sample in Hsiao et al. (2019) ($\sim$10,000-12,000 km s^{-1}), but still consistent with the HVFs of Ca II IRT. Nonetheless, no significant carbon absorption is detected in the optical band.

The Fe II features in SNe Ia usually start to develop roughly three weeks after the peak, which is about the same phase as we obtained our GNIRS spectrum. Two Fe II lines, $\lambda 0.9998\,\mu$m and $\lambda 1.0500\,\mu$m, are actually visible on the blue/red wings of the $1\,\mu$m feature. The Fe II $\lambda 1.0863\,\mu$m line is not yet seen in the GNIRS spectrum. They correspond to an expansion velocity of $\approx$8,000 km s^{-1}, which is consistent with the PVFs of the Ca II IRT at the same epoch. They also match the same two lines for normal SNe Ia (Marion et al. 2009), making the identification more reliable. Obviously, these two Fe II features are wider and shallower than the strong feature between them. We fit the 1 μm feature with three Gaussian profiles. Two of them are set to be the blueshifted Fe II $\lambda 0.9998\,\mu$m and $\lambda 1.0500\,\mu$m, and the other is an uncorrelated Gaussian profile which mainly describes the absorption in the center. We find that the shallower and wider Fe II lines only make up ∼40% of the total equivalent width, and the rest ∼60% comes from the central feature, which cannot be accounted for by any Fe II feature at the same velocity. Given the similarity of the Fe-group line-blanketing between the GNIRS spectrum with the spectrum of SN 2004da at +25 days, the distribution of Fe-group elements inside each supernova ejecta should be somehow similar as normal SNe Ia, so the central region of the 1 μm feature is not likely to be associated with Fe II either.

While the nature of the 1 μm feature remains uncertain, other He-shell DDet candidates also seem to show similar complexity in this region. In the currently small sample of six candidates, three objects (SN 2016jhr, SN 2018aoz, and SN 2019ofm) do not have any available NIR spectra, while the other three (at quite different phases though) all exhibit strong absorption features near 1 μm, as shown in Figure 5. SN 2016hnk has two deep absorption features around 1.02 μm and 1.17 μm, both are at a longer wavelength than the 1μm feature in SN 2020jgb. Galbany et al. (2019) suggest both of them could be caused by Fe II, though they are deeper than in other SNe Ia. The velocity of the 1.02 μm feature is ≈21,000 km s^{-1} assuming a He I $\lambda 1.0830\,\mu$m origin, which, just like SN 2020jgb, is about the same as the HVFs of the Ca II IRT in the optical spectra (see Figure 4). The PVFs of the Ca II IRT of both SNe have a similar expansion velocity of ≈10,000 km s^{-1}. Such a consistency in velocities in also seen in SN 2018byg (see Figure 4). But given the exotic width and lower signal-to-noise ratio in the 1 μm feature, the exact line velocity is hard to determine. It is likely to be a mixture of several different lines.

Dong et al. (2022) recently proposed another thick He-shell DDet candidate, SN 2016dsg, with an absorption line around 0.97-1.05 μm in a low-SNR NIR spectrum at +16.6 days[4]. Assuming He I $\lambda 1.0830\,\mu$m origin, the minimum of the absorption profile (at ≈1.03 μm, see Figure 4 in Dong et al. 2022) corresponds to an expansion velocity of ≈15,000 km s^{-1}. This is lower than the 1 μm features in SN 2020jgb and SN 2016hnk assuming their He I origin. Interestingly, SN 2016dsg shows the least prominent HVFs of Ca II IRT among the four, which also has a low velocity of ≈15,000 km s^{-1}. Once again, the scenario where both the unburnt helium and the high velocity calcium are located at the outermost shell is favored.

Unfortunately, none of the spectra for SN 2016dsg, SN 2016hnk, or SN 2018byg covers the 2 μm region, thus it is not possible to identify the presence of helium decisively. But if the 1 μm feature of the these objects are of the same origin, they are more likely to be correlated with the high velocity ejecta lying in the outmost region in the supernovae, because at least for SN 2020jgb and SN 2016hnk, the difference in their photospheric velocities cannot explain the discrepancy in their line velocities of the 1 μm feature. Then helium is still a promising candidate to cause strong absorption near 1 μm for these sub-luminous He-shell DDet SNe Ia.

In conclusion, from all the He-shell DDet candidates with NIR spectra available, we have detected strong absorption features near 1 μm, which is not seen in normal SNe Ia. Indeed, these candidates have their NIR spectra taken at different epochs, hence each 1 μm feature can be of completely unrelated origin. Had they all originate from He I $\lambda 1.0830\,\mu$m, there would still be large diversity in the corresponding expansion velocities. This is to be confirmed in a more complete NIR spectral sequence in future He-shell DDet SNe Ia. Nonetheless, the seemingly ubiquitous 1 μm feature in various phases is possibly a distinctive attribute against normal SNe Ia.

4. HOST GALAXY

We obtained a DEIMOS spectrum of the host galaxy, PSO J175312.663+005122.078, on 2022 March 31. The host exhibits strong, narrow emission lines including Hα, Hβ, [N II] λ6583, [O III] λ5007, and [S II] λ6716 & λ6731. By fitting all these emission features with Gaussian profiles we obtain an average redshift of $z = 0.0309 \pm 0.0003$. With the diagnostic emission line equivalent width ratios (log [N II]/Hα $= -1.19 \pm 0.07$ and log [O III]/Hβ $= 0.53 \pm 0.06$), the host is consistent with star-forming galaxies in the BPT diagram (Baldwin et al. 1981; Veilleux & Osterbrock 1987).

We model the detailed properties of the host galaxy using `prospector` (Johnson et al. 2021), a package for principled inference of stellar population properties using photometric and/or spectroscopic data. The input data included the Galactic extinction corrected DEIMOS spectrum, as well as the archival photometric data from the Panoramic Survey Telescope and Rapid Response System (Pan-STARRS; Chambers et al. 2016, r, i, z Kron magnitudes) and the VISTA Hemisphere Survey (VHS; McMahon et al. 2013, J and K$_s$ Petrosian magnitudes). In the best fit, the estimated stel-

[4] SN 2016dsg was discovered declining. The phase is relative to the discovery time.

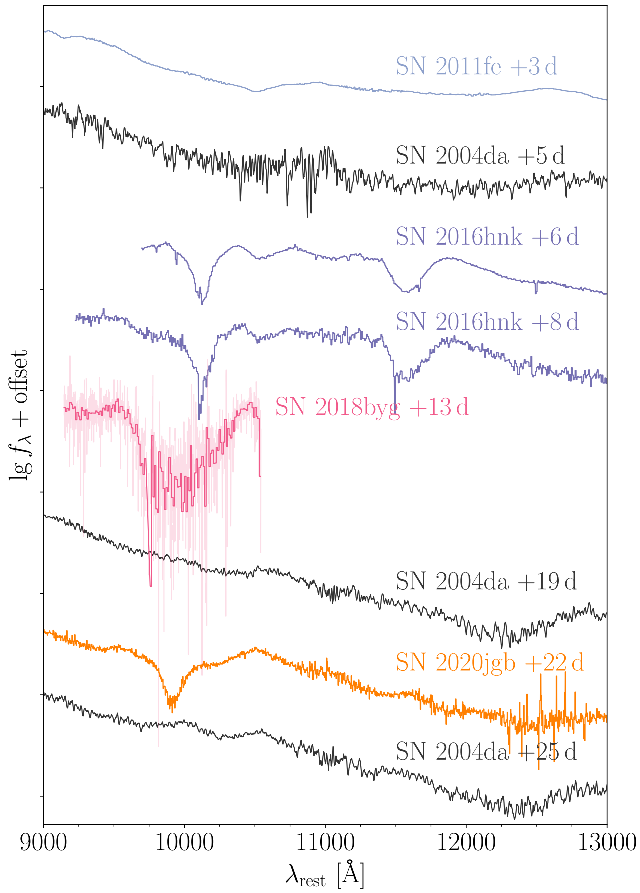

Figure 5. The NIR spectra (9000 to 13000 Å) of a few normal SNe Ia (SN 2011fe and SN 2004da) and three He-shell DDet candidates, which are all sub-luminous SNe Ia (SN 2016hnk, SN 2018byg, and this source, SN 2020jgb). Other than the spectrum of SN 2004da, all spectroscopic data are obtained from the WISEReP repository (Yaron & Gal-Yam 2012).

lar mass is $\log(M_*\,[\mathrm{M}_\odot]) = 7.79^{+0.07}_{-0.06}$, and the specific star-formation rate (sSFR) is $\log(\mathrm{sSFR}\,[\mathrm{yr}^{-1}]) = -10.25^{+0.09}_{-0.08}$, with the uncertainties denoting the 68% credible regions.

In Figure 4, we show the sSFR and the stellar mass for the host galaxies of our six He-shell DDet candidates. Again using `prospector`, we fit the stellar properties for all the other candidates with optical spectra from the Sloan Digital Sky Survey (SDSS; York et al. 2000) and photometry from the DESI Legacy Imaging Surveys (Dey et al. 2019, g, r, z, W_1, W_2, W_3, W_4 magnitudes). With mid-infrared photometry available, `prospector` can better estimate the overall dust extinction in the host galaxy and the contribution of an active galactic nucleus (AGN) to the spectral energy distribution (SED). Unfortunately, two (SN 2016hnk and SN 2019ofm) out of six hosts are close-by ($z \lesssim 0.03$) late-type galaxies with extended, spatially resolvable spiral structures. In both surveys, only photons from their red, concentrated bulges were fed to the detectors, while the lights from the blue, diffusive star-forming regions were completely missed. We would inevitably underestimate their SFR should we naively fit the SEDs from these surveys. Therefore, for the host of SN 2016hnk, we adopt the results in Galbany et al. (2019) as part of the PMAS/PPak Integral-field Supernova Hosts Compilation (PISCO; Galbany et al. 2018), where the photons from the H II regions in the spiral arms were also collected using integral field spectroscopy (IFS). For the host of SN 2019ofm, there are no IFS data available, so we still show our best-fit stellar mass and sSFR in Figure 4, with the caveat that the sSFR should be regarded as a lower limit. The host of SN 2018aoz (NGC 3923) is a local ($z = 0.00580$) early-type galaxy and is outside the SDSS footprint, so we adopt its stellar population properties from the Census of the Local Universe (CLU) catalog [AAM: References?].

The recent study on SN 2016dsg and OGLE-2013-SN-079 (Dong et al. 2022) enlarges the sample of thick He-shell DDet candidates. Similar to SN 2018byg, both of the them reside in the outskirts of early-type galaxies which are >10 kpc away from the host centers, indicating an origin in old stellar populations. A projected host offset $\gtrsim$10 kpc is also seen in SN 2016jhr, SN 2018aoz, and SN 2019ofm, whereas the hosts of SN 2016jhr and SN 2019ofm are star-forming galaxies. SN 2016hnk, on the contrary, has a smaller projected host offset of ∼4 kpc and a potential origin in an H II region with ongoing star-formation (Galbany et al. 2019). SN 2020jgb is the first He-shell DDet candidate in a star-forming dwarf galaxy. It has has the smallest projected physical offset (∼0.2 kpc) yet to know.

Given the limited sample size yet, the host environments of the He-shell DDet candidates have started to show diversity. This is true for both thin He-shell objects of normal luminosity (SN 2016jhr in a star-forming host; SN 2018aoz in a quenched host) and thick He-shell, sub-luminous objects (SN 2020jgb in a star-forming host; SN 2016dsg, SN 2018byg, and OGLE-2013-SN-079 in quenched hosts), even when the natures of SN 2016hnk and SN 2019ofm remain ambiguous. In this sense, the He-shell DDet sample resembles the SNe Ia population in general, which can occur in both star-forming and quenched galaxies (e.g., Sullivan et al. 2006; Smith et al. 2012). But such a diversity in host environments is very different from some other types thermonuclear supernovae, such as Type-Iax supernovae (SNe Iax) which almost only appear in star-forming galaxies, or SN 1991bg-like and SN 2002es-like objects, which prefer old stellar environments (see the review in Jha et al. 2019). Most SNe in our sample show a relative large host galaxy offset, which has also been observed in many Ca-rich transients (Lunnan et al. 2017), with typical projected offsets being ∼10-100 kpc (De et al. 2020). Some dynamical formation channels have been proposed to explain the remote locations of Ca-rich transients, such that WD binaries would need to be hardened and ejected by globular clusters (Shen et al. 2019) or supermassive black holes (Foley 2015) before explosions, which may also be the case for some, if any all, of He-shell DDet SNe. Other DDet SNe, SN 2020jgb being the most unambiguous example, are located in star-forming regions and are thus highly likely to be formed *in situ*. Two recently discovered subdwarf B binaries with WD companions which were found in young stellar populations could be promising progenitor systems (Geier et al. 2013; Kupfer et al. 2022).

The robust detection of He-shell DDet SNe in star-formation regions also agrees with independent studies on SNe Ia progenitors using stellar metallicity observations. de los Reyes et al. (2020), by studying the manganese abundances in dwarf spheroidal satellites of the Milky Way, argue that sub-M_{Ch} SNe Ia dominates the chemical evolution of a galaxy, while near-M_{Ch} SNe tend to take over at later times, indicating that observationally, sub-M_{Ch} SNe Ia might have a stronger preference towards younger stellar populations than near-M_{Ch} SNe Ia. He-shell DDet is one of the most favored channel to ignite a sub-M_{Ch} WD, which could produce both normal and sub-luminous SNe Ia. Consequently, we would expect the majority of exploded SNe Ia in star-forming galaxies (at least the dwarfs) would undergo DDet. We note that while SN 2020jgb is the first confirmed He-shell DDet SN in a star-forming dwarf, which indicates that thick shell DDet SNe might be intrinsically rare, the same may not be true for thin shell DDet SNe since they would look just as *normal* in both photometric and spectroscopic evolution a few days after explosions (Ni et al. 2022). Unfortunately, few of them are observed in such an early phase to date (SN 2016jhr and SN 2018aoz being two of them), thus we might have missed a great number of He-shell DDet SNe. With more efficient time domain surveys kicking in in the near future and prompt follow-up observations being increasingly available (**also need some references**), a systematic studies on the infant SNe Ia will help confirm this implication. [AAM: Do you think we should put this paragraph here or in the discussion section?]

5. MODEL COMPARISONS

A few sentences from Abi describing the models.

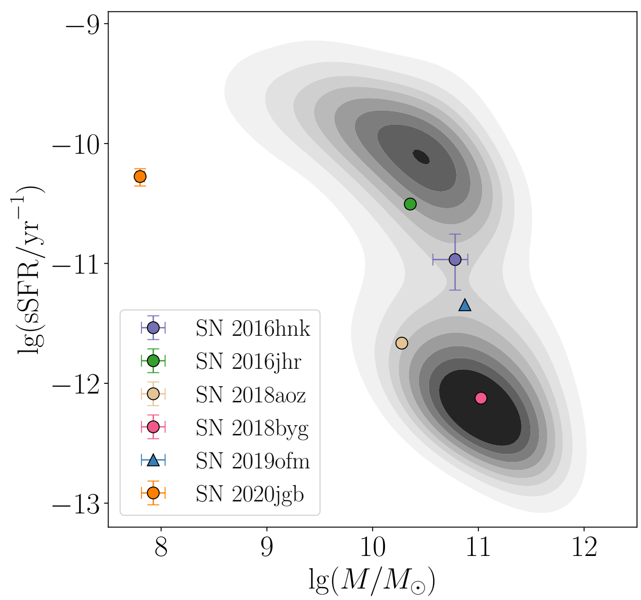

Figure 6. The specific star-formation rate (sSFR) and the stellar mass for the host galaxies of He-shell DDet candidates. The properties for the hosts of SN 2016hnk and SN 2018aoz are taken from Galbany et al. (2019) and the CLU catalog [AAM: References?], respectively. For the sSFR in the host of SN 2019ofm, only a lower limit is shown (the triangle). The background is a sample of galaxies from the SDSS MPA-JHU DR8 catalog (Kauffmann et al. 2003; Brinchmann et al. 2004). Galaxies with BPT classification as AGNs or LINERs are excluded, since certain spectral features (e.g., Hα emission) due to nuclear activities might be misinterpreted as star formation.

In Figure 5, we show the comparison of the photometric and spectroscopic features of SN 2020jgb with DDet models from Polin et al. (2019). The peak luminosity reflects the total progenitor mass (C/O core + He shell), and we find models with a total mass of 0.95 $M_{\odot}$ generally reproduce the r-band peak brightness well. Thus in Figure 5, the total mass is fixed to be 0.95 $M_{\odot}$ in all models. The overall r-band photometric evolution is best fit by the model with a 0.87 $M_{\odot}$ C/O core and a 0.08 $M_{\odot}$ He shell, while all three models underestimate the g-band brightness after the peak. This deviation may be attributed to a variety of factors on handling the explosion and radiative transfer. First, throughout the simulations we assume local thermodynamic equilibrium (LTE), which is not valid once the ejecta becomes optically thin. Typically the bulk ejecta of a sub-Chandrasekhar SNe Ia remains optically thick for ∼30 days since the explosion. But in modeling the brightness g-band, the LTE assumption is even more tricky, because the major opacity in g-band comes from the Fe-group line-blanketing in the outermost ejecta, where the optical depth may evolve differently from that at the photosphere. Hence the LTE condition may quickly become inapplicable. Furthermore, our 1-D He shell model is not capable to capture the multi-dimensional effects in the explosion such as asymmetries. The viewing angle is known to have a significant influence on the observed light curves (Kromer et al. 2010; Sim et al. 2012; Gronow et al. 2020; Shen et al. 2021), especially in bluer bands where the line-blanketing depends sensitively on the distribution of He-shell ashes (Shen et al. 2021). In previous studies on other DDet objects, the g-band brightness is systematically under-predicted shortly after the peak, despite the fact that redder bands can be fit decently (e.g. Jiang et al. 2017; Jacobson-Galán et al. 2020).

The model which best fits the photometry ($0.87\,\mathrm{M}_\odot + 0.08\,\mathrm{M}_\odot$) also reproduces the major absorption features (e.g., Fe-group line-blanketing, Si II λ6355, PVFs of Ca II IRT) and the corresponding expansion velocities near the peak light. However, we are not able to fit the continua in g-, r-, and z-bands simultaneously, and the strong Ca II HVFs are not seen in the best-fit spectrum. These discrepancies could also be due to the asymmetry in the DDet, that SN 2020jgb was observed fairly close to the ignition point, where the abundances of Fe-group elements and high velocity calcium synthesized in the shell could be much higher than an angle-averaged 1-D model would predict. In addition, the predicted Si II λ5972 does not show up in the observed spectrum.

Conclusions from the model comparison.

6. DISCUSSION AND CONCLUSIONS

In the paper, we have presented the observations of SN 2020jgb, a sub-luminous SN Ia. Putting together its unusual red colors and strong line-blanketing in the spectra near peak light, we show its peculiar nature as a SN Ia. It bears a high degree of resemblance to SN 2018byg (De et al. 2019), whose observational properties could be explained by the detonation of a shell of helium on a sub-M_{Ch}WD. Fitting the light curve of SN 2020jgb to a grid of models in Polin et al. (2019), we show a $\approx$0.87 $\mathrm{M}_\odot$ WD beneath a $\approx$0.08 $\mathrm{M}_\odot$ He-shell would be a reasonable estimate on its progenitor properties.

A high-SNR NIR spectrum obtained three weeks after the peak light shows a prominent absorption feature near 1 μm, which could be produced by the unburnt helium (He I λ1.0830 μm) in the outermost ejecta expanding at a high velocity ($\approx$26,000 $\mathrm{km\,s^{-1}}$). At the same epoch, the Ca II IRT also exhibits similarly high velocities ($\approx$24,000 $\mathrm{km\,s^{-1}}$). By now, we have a very small sample of four candidate He-shell DDet SNe which have NIR spectra observed. Interesting, all of them show deep absorption features near 1 μm, which, if assumed to have a helium origin, would be expanding very a similar velocity as the high velocity component of Ca II IRT, despite the huge diversity in the Ca II IRT velocity (from $\approx$15,000 $\mathrm{km\,s^{-1}}$ in SN 2016dsg to $\approx$24,000 $\mathrm{km\,s^{-1}}$ in SN 2020jgb) in our tiny sample. Such a consistency in velocities of absorption lines would be naturally explained if it is the unburnt helium and the newly synthesized calcium from the He-shell that produce these line features. However, we could not find unambiguous evidence for other He I absorption lines, such as He I λ2.0581 μm, so we are not drawing a strong conclusion of helium detection in SN 2020jgb. Nonetheless, we discuss other potential strong lines (Mg II, C I, Fe II) that may cause the 1 μm feature, but have found them also not that likely. Helium is still the most promising candidate.

This paper provides a framework of robust He I detection in He-shell DDet SNe. Ideally, one will need a NIR spectrum covering both the 1 μm and 2 μm regions in search of the He I λ1.0830 μm and λ2.0581 μm features. Since the He I λ2.0581 μm is weaker or even invisible when the He-shell is thin (Boyle et al. 2017), and could be blended with strong telluric lines, one should not always expect to see significant absorption features near 2 μm. For those with a clear 1 μm feature, one can calculate the required velocity for an origin in He I λ1.0830 μm, to see if it is comparable with the velocity with the HVFs in the Ca II IRT at a similar phase. While the detonation recipe in a DDet model and the viewing angles would all affect the observed He I velocity, we still expect the elements along the line-of-sight to expand at a similar pace, if they all have a He-shell origin. Excluding the possibility of other strong lines is also necessary, especially when the NIR spectrum is obtained before the peak of the SN, when there can be strong Mg II and C I absorption (Hsiao et al. 2019).

In the tiny sample of DDet candidates to date, we have seen diversity in observational properties, including the peak luminosity, color evolution, chemical abundances and line velocities, which could be explained by a large variety of He-shell masses, WD masses, viewing angles, and the initial chemical compositions in the shell. In addition, they are discovered in both old and young stellar populations, SN 2020jgb being the first unambiguous thick He-shell DDet candidate in a star-forming galaxy, suggesting their possible origins in a mixture of formation channels and progenitor systems.

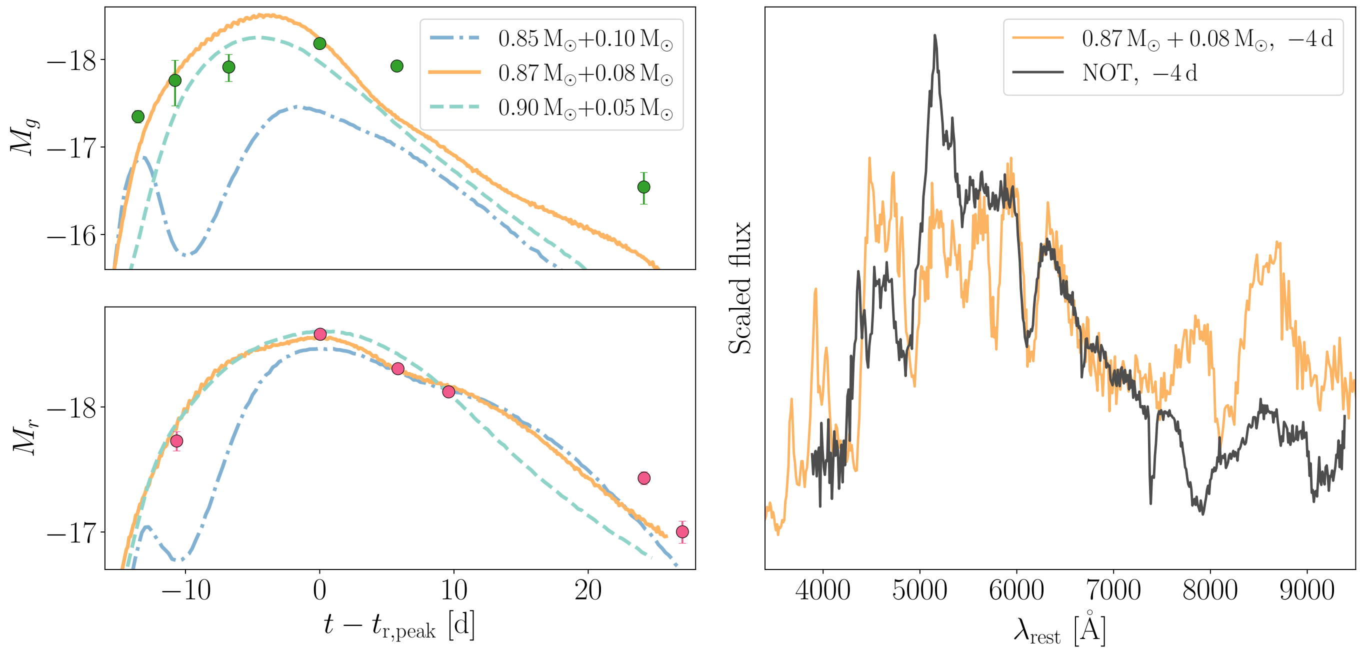

Figure 7. *Left:* Comparison of the photometric evolution of SN 2020jgb with the He-shell DDet models from Polin et al. (2019). The model parameters are indicated in the legend as (C/O core mass + He shell mass). The upper (lower) panel shows the evolution in g-band (r-band) absolute magnitudes. *Right:* Comparison of the spectrum of SN 2020jgb with the $0.87\,M_\odot$ C/O core + $0.08\,M_\odot$ He-shell DDet model before peak luminosity. Each spectrum is normalized by the median flux between 6500 and 7500 Å, and binned with a size of 10 Å. The synthetic spectrum 4 days before the the r-band peak best matches the NOT spectrum (Galactic extinction corrected), which was obtained ∼4 days before the r_{ZTF}-band peak. All the phases have been rescaled to the host galaxy rest frame.

Facility: PO:1.2m (ZTF), PO:1.5m (SEDM), Hale (DBSP), NOT (ALFOSC), Shane (Kast Double spectrograph), Keck:I (LRIS), Keck:II (DEIMOS), Gemini:Gillett (GNIRS)

Software: `astropy` (Astropy Collaboration et al. 2013, 2018), `emcee` (Foreman-Mackey et al. 2013), `matplotlib` (Hunter 2007), `prospector` (Johnson et al. 2021), `PypeIt` (Prochaska et al. 2020), `scikit-learn` (Pedregosa et al. 2011), `scipy` (Virtanen et al. 2020), `seaborn` (Waskom 2021).

REFERENCES

Astropy Collaboration, Robitaille, T. P., Tollerud, E. J., et al. 2013, A&A, 558, A33, doi: 10.1051/0004-6361/201322068

Astropy Collaboration, Price-Whelan, A. M., Sipőcz, B. M., et al. 2018, AJ, 156, 123, doi: 10.3847/1538-3881/aabc4f

Baldwin, J. A., Phillips, M. M., & Terlevich, R. 1981, PASP, 93, 5, doi: 10.1086/130766

Bellm, E. C., Kulkarni, S. R., Graham, M. J., et al. 2019, PASP, 131, 018002, doi: 10.1088/1538-3873/aaecbe

Bildsten, L., Shen, K. J., Weinberg, N. N., & Nelemans, G. 2007, ApJL, 662, L95, doi: 10.1086/519489

Blagorodnova, N., Neill, J. D., Walters, R., et al. 2018, PASP, 130, 035003, doi: 10.1088/1538-3873/aaa53f

Boyle, A., Sim, S. A., Hachinger, S., & Kerzendorf, W. 2017, A&A, 599, A46, doi: 10.1051/0004-6361/201629712

Brinchmann, J., Charlot, S., White, S. D. M., et al. 2004, MNRAS, 351, 1151, doi: 10.1111/j.1365-2966.2004.07881.x

Bulla, M., Miller, A. A., Yao, Y., et al. 2020, ApJ, 902, 48, doi: 10.3847/1538-4357/abb13c

Carrick, J., Turnbull, S. J., Lavaux, G., & Hudson, M. J. 2015, MNRAS, 450, 317, doi: 10.1093/mnras/stv547

Cenko, S. B., Fox, D. B., Moon, D.-S., et al. 2006, PASP, 118, 1396, doi: 10.1086/508366

Chambers, K. C., Magnier, E. A., Metcalfe, N., et al. 2016, arXiv e-prints, arXiv:1612.05560. https://arxiv.org/abs/1612.05560

Dahiwale, A., & Fremling, C. 2020, Transient Name Server Classification Report, 2020-1624, 1
De, K., Kasliwal, M. M., Polin, A., et al. 2019, The Astrophysical Journal, 873, L18, doi: 10.3847/2041-8213/ab0aec
De, K., Kasliwal, M. M., Tzanidakis, A., et al. 2020, The Astrophysical Journal, 905, 58, doi: 10.3847/1538-4357/abb45c
De, K., Kasliwal, M. M., Tzanidakis, A., et al. 2020, ApJ, 905, 58, doi: 10.3847/1538-4357/abb45c
de los Reyes, M. A. C., Kirby, E. N., Seitenzahl, I. R., & Shen, K. J. 2020, ApJ, 891, 85, doi: 10.3847/1538-4357/ab736f
Deckers, M., Maguire, K., Magee, M. R., et al. 2022, MNRAS, 512, 1317, doi: 10.1093/mnras/stac558
Dessart, L., & Hillier, D. J. 2015, MNRAS, 447, 1370, doi: 10.1093/mnras/stu2520
Dey, A., Schlegel, D. J., Lang, D., et al. 2019, AJ, 157, 168, doi: 10.3847/1538-3881/ab089d
Dong, Y., Valenti, S., Polin, A., et al. 2022, arXiv e-prints, arXiv:2206.07065. https://arxiv.org/abs/2206.07065
Duev, D. A., Mahabal, A., Masci, F. J., et al. 2019, MNRAS, 489, 3582, doi: 10.1093/mnras/stz2357
Elias, J. H., Vukobratovich, D., Andrew, J. R., et al. 1998, in Society of Photo-Optical Instrumentation Engineers (SPIE) Conference Series, Vol. 3354, Infrared Astronomical Instrumentation, ed. A. M. Fowler, 555–565, doi: 10.1117/12.317281
Faber, S. M., Phillips, A. C., Kibrick, R. I., et al. 2003, in Society of Photo-Optical Instrumentation Engineers (SPIE) Conference Series, Vol. 4841, Instrument Design and Performance for Optical/Infrared Ground-based Telescopes, ed. M. Iye & A. F. M. Moorwood, 1657–1669, doi: 10.1117/12.460346
Filippenko, A. V., Richmond, M. W., Branch, D., et al. 1992, AJ, 104, 1543, doi: 10.1086/116339
Fink, M., Röpke, F. K., Hillebrandt, W., et al. 2010, A&A, 514, A53, doi: 10.1051/0004-6361/200913892
Fitzpatrick, E. L. 1999, PASP, 111, 63, doi: 10.1086/316293
Foley, R. J. 2015, MNRAS, 452, 2463, doi: 10.1093/mnras/stv789
Foreman-Mackey, D., Hogg, D. W., Lang, D., & Goodman, J. 2013, PASP, 125, 306, doi: 10.1086/670067
Fremling, C. 2020, Transient Name Server Discovery Report, 2020-1247, 1
Galbany, L., Anderson, J. P., Sánchez, S. F., et al. 2018, ApJ, 855, 107, doi: 10.3847/1538-4357/aaaf20
Galbany, L., Ashall, C., Höflich, P., et al. 2019, Astronomy & Astrophysics, 630, A76, doi: 10.1051/0004-6361/201935537
Geier, S., Marsh, T. R., Wang, B., et al. 2013, A&A, 554, A54, doi: 10.1051/0004-6361/201321395
Graham, M. J., Kulkarni, S. R., Bellm, E. C., et al. 2019, PASP, 131, 078001, doi: 10.1088/1538-3873/ab006c
Gronow, S., Collins, C., Ohlmann, S. T., et al. 2020, A&A, 635, A169, doi: 10.1051/0004-6361/201936494
Guillochon, J., Parrent, J., Kelley, L. Z., & Margutti, R. 2017, ApJ, 835, 64, doi: 10.3847/1538-4357/835/1/64
Hsiao, E. Y., Phillips, M. M., Marion, G. H., et al. 2019, PASP, 131, 014002, doi: 10.1088/1538-3873/aae961
Hunter, J. D. 2007, Computing in Science and Engineering, 9, 90, doi: 10.1109/MCSE.2007.55
Inserra, C., Sim, S. A., Wyrzykowski, L., et al. 2015, ApJL, 799, L2, doi: 10.1088/2041-8205/799/1/L2
Jacobson-Galán, W. V., Polin, A., Foley, R. J., et al. 2020, The Astrophysical Journal, 896, 165, doi: 10.3847/1538-4357/ab94b8
Jha, S. W., Maguire, K., & Sullivan, M. 2019, Nature Astronomy, 3, 706, doi: 10.1038/s41550-019-0858-0
Jiang, J.-a., Doi, M., Maeda, K., et al. 2017, Nature, 550, 80, doi: 10.1038/nature23908
Johnson, B. D., Leja, J., Conroy, C., & Speagle, J. S. 2021, ApJS, 254, 22, doi: 10.3847/1538-4365/abef67
Kauffmann, G., Heckman, T. M., White, S. D. M., et al. 2003, MNRAS, 341, 33, doi: 10.1046/j.1365-8711.2003.06291.x
Kromer, M., Sim, S. A., Fink, M., et al. 2010, ApJ, 719, 1067, doi: 10.1088/0004-637X/719/2/1067
Kupfer, T., Bauer, E. B., van Roestel, J., et al. 2022, ApJL, 925, L12, doi: 10.3847/2041-8213/ac48f1
Livne, E. 1990, ApJL, 354, L53, doi: 10.1086/185721
Livne, E., & Arnett, D. 1995, ApJ, 452, 62, doi: 10.1086/176279
Lunnan, R., Kasliwal, M. M., Cao, Y., et al. 2017, ApJ, 836, 60, doi: 10.3847/1538-4357/836/1/60
Maguire, K., Sullivan, M., Pan, Y. C., et al. 2014, MNRAS, 444, 3258, doi: 10.1093/mnras/stu1607
Mahabal, A., Rebbapragada, U., Walters, R., et al. 2019, PASP, 131, 038002, doi: 10.1088/1538-3873/aaf3fa
Maoz, D., Mannucci, F., & Nelemans, G. 2014, ARA&A, 52, 107, doi: 10.1146/annurev-astro-082812-141031
Marion, G. H., Höflich, P., Gerardy, C. L., et al. 2009, AJ, 138, 727, doi: 10.1088/0004-6256/138/3/727
Masci, F. J., Laher, R. R., Rusholme, B., et al. 2019, PASP, 131, 018003, doi: 10.1088/1538-3873/aae8ac
Matheson, T., Filippenko, A. V., Barth, A. J., et al. 2000, AJ, 120, 1487, doi: 10.1086/301518
McMahon, R. G., Banerji, M., Gonzalez, E., et al. 2013, The Messenger, 154, 35

Miller, J., & Stone, R. 1994, The Kast Double Spectograph, Lick Observatory technical reports (University of California Observatories/Lick Observatory). https://books.google.com/books?id=QXk2AQAAIAAJ

Ni, Y. Q., Moon, D.-S., Drout, M. R., et al. 2022, Nature Astronomy, doi: 10.1038/s41550-022-01603-4

Nomoto, K. 1982a, ApJ, 253, 798, doi: 10.1086/159682

—. 1982b, ApJ, 257, 780, doi: 10.1086/160031

Nugent, P. E., Sullivan, M., Cenko, S. B., et al. 2011, Nature, 480, 344, doi: 10.1038/nature10644

Oke, J. B., & Gunn, J. E. 1982, PASP, 94, 586, doi: 10.1086/131027

Oke, J. B., Cohen, J. G., Carr, M., et al. 1995, PASP, 107, 375, doi: 10.1086/133562

Patterson, M. T., Bellm, E. C., Rusholme, B., et al. 2019, PASP, 131, 018001, doi: 10.1088/1538-3873/aae904

Pedregosa, F., Varoquaux, G., Gramfort, A., et al. 2011, Journal of Machine Learning Research, 12, 2825

Polin, A., Nugent, P., & Kasen, D. 2019, ApJ, 873, 84, doi: 10.3847/1538-4357/aafb6a

—. 2021, ApJ, 906, 65, doi: 10.3847/1538-4357/abcccc

Poznanski, D., Ganeshalingam, M., Silverman, J. M., & Filippenko, A. V. 2011, MNRAS, 415, L81, doi: 10.1111/j.1745-3933.2011.01084.x

Prochaska, J. X., Hennawi, J. F., Westfall, K. B., et al. 2020, Journal of Open Source Software, 5, 2308, doi: 10.21105/joss.02308

Prochaska, J. X., Hennawi, J., Cooke, R., et al. 2020, pypeit/PypeIt: Release 1.0.0, v1.0.0, Zenodo, doi: 10.5281/zenodo.3743493

Schlafly, E. F., & Finkbeiner, D. P. 2011, ApJ, 737, 103, doi: 10.1088/0004-637X/737/2/103

Shahbandeh, M., Hsiao, E. Y., Ashall, C., et al. 2022, ApJ, 925, 175, doi: 10.3847/1538-4357/ac4030

Shen, K. J., Boos, S. J., Townsley, D. M., & Kasen, D. 2021, ApJ, 922, 68, doi: 10.3847/1538-4357/ac2304

Shen, K. J., Kasen, D., Miles, B. J., & Townsley, D. M. 2018, ApJ, 854, 52, doi: 10.3847/1538-4357/aaa8de

Shen, K. J., & Moore, K. 2014, ApJ, 797, 46, doi: 10.1088/0004-637X/797/1/46

Shen, K. J., Quataert, E., & Pakmor, R. 2019, ApJ, 887, 180, doi: 10.3847/1538-4357/ab5370

Silverman, J. M., Vinkó, J., Marion, G. H., et al. 2015, MNRAS, 451, 1973, doi: 10.1093/mnras/stv1011

Sim, S. A., Fink, M., Kromer, M., et al. 2012, MNRAS, 420, 3003, doi: 10.1111/j.1365-2966.2011.20162.x

Sim, S. A., Röpke, F. K., Hillebrandt, W., et al. 2010, ApJL, 714, L52, doi: 10.1088/2041-8205/714/1/L52

Smith, M., Nichol, R. C., Dilday, B., et al. 2012, ApJ, 755, 61, doi: 10.1088/0004-637X/755/1/61

Sullivan, M., Le Borgne, D., Pritchet, C. J., et al. 2006, ApJ, 648, 868, doi: 10.1086/506137

Veilleux, S., & Osterbrock, D. E. 1987, ApJS, 63, 295, doi: 10.1086/191166

Virtanen, P., Gommers, R., Oliphant, T. E., et al. 2020, Nature Methods, 17, 261, doi: 10.1038/s41592-019-0686-2

Waskom, M. L. 2021, Journal of Open Source Software, 6, 3021, doi: 10.21105/joss.03021

Woosley, S. E., Taam, R. E., & Weaver, T. A. 1986, ApJ, 301, 601, doi: 10.1086/163926

Woosley, S. E., & Weaver, T. A. 1994, ApJ, 423, 371, doi: 10.1086/173813

Yaron, O., & Gal-Yam, A. 2012, PASP, 124, 668, doi: 10.1086/666656

York, D. G., Adelman, J., Anderson, John E., J., et al. 2000, AJ, 120, 1579, doi: 10.1086/301513

Zackay, B., Ofek, E. O., & Gal-Yam, A. 2016, ApJ, 830, 27, doi: 10.3847/0004-637X/830/1/27